
PHYRECON: Physically Plausible Neural Scene Reconstruction

Junfeng Ni^{1,2*}, Yixin Chen^{1*}, Bohan Jing¹, Nan Jiang^{1,3}, Bin Wang¹,
Bo Dai¹, Yixin Zhu³, Song-Chun Zhu^{1,2,3}, Siyuan Huang¹

* indicates equal contribution

¹ National Key Laboratory of General Artificial Intelligence, BIGAI

² Tsinghua University ³ Peking University

<https://phyrecon.github.io/>

Abstract

While neural implicit representations have gained popularity in multi-view 3D reconstruction, previous work struggles to yield physically plausible results, thereby limiting their applications in physics-demanding domains like embodied AI and robotics. The lack of plausibility originates from both the absence of physics modeling in the existing pipeline and their inability to recover intricate geometrical structures. In this paper, we introduce PHYRECON, which stands as the first approach to harness both differentiable rendering and differentiable physics simulation to learn implicit surface representations. Our framework proposes a novel differentiable particle-based physical simulator seamlessly integrated with the neural implicit representation. At its core is an efficient transformation between SDF-based implicit representation and explicit surface points by our proposed algorithm, Surface Points Marching Cubes (SP-MC), enabling differentiable learning with both rendering and physical losses. Moreover, we model both rendering and physical uncertainty to identify and compensate for the inconsistent and inaccurate monocular geometric priors. The physical uncertainty additionally enables a physics-guided pixel sampling to enhance the learning of slender structures. By amalgamating these techniques, our model facilitates efficient joint modeling with appearance, geometry, and physics. Extensive experiments demonstrate that PHYRECON significantly outperforms all state-of-the-art methods in terms of reconstruction quality. Our reconstruction results also yield superior physical stability, verified by Isaac Gym, with at least a 40% improvement across all datasets, opening broader avenues for future physics-based applications.

1 Introduction

3D scene reconstruction stands as a fundamental task in computer vision, with various applications spanning graphics, animation, VR/AR, *etc.*. Despite recent progress [41, 30, 44, 4, 34], the physical plausibility of the reconstruction results remains inadequate. Previous attempts to incorporate physics constraints often rely on hand-crafted collision loss under simplified representation, *e.g.*, 3D bounding boxes [11, 2] or 3D occupancy [72]. Building upon the advancements of neural implicit representations [39], previous methods [18, 57, 69] have capitalized on multi-view images and their monocular cues for fine-grained 3D geometry recovery via volume rendering [10]. However, the notable gap persists, as most previous work in neural scene reconstruction has overlooked the crucial aspects of physical plausibility. The lack of consideration and consequently their struggle to attain physically plausible results, significantly restrict their applicability in physics-demanding tasks like embodied AI [17, 1, 27] and robotics [15, 24, 54].

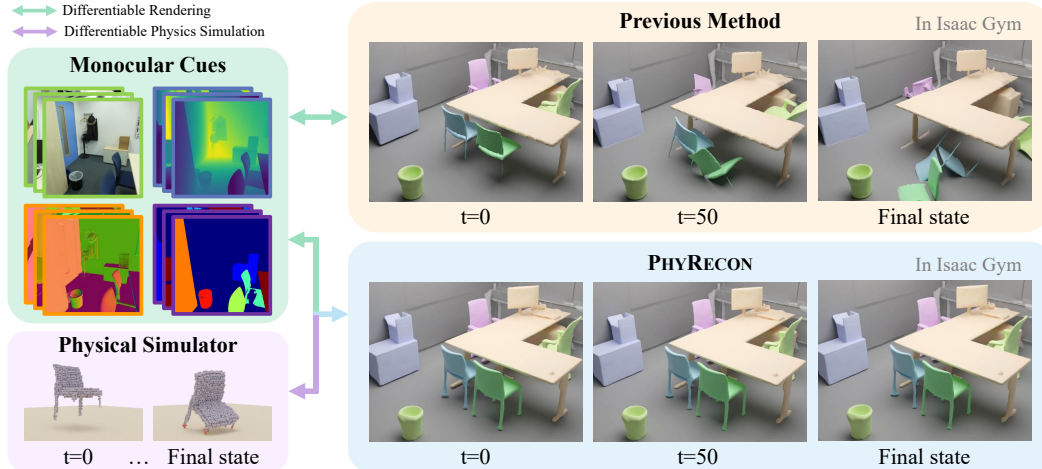


Figure 1: **Illustration of PHYRECON.** We leverage both differentiable physics simulation and differentiable rendering to learn implicit surface representation. Results from previous method [29] fail to remain stable in physical simulators and recover intricate geometries, while PHYRECON achieves significant improvements in both reconstruction quality and physical plausibility.

The inability to achieve physically plausible reconstruction stems from two fundamental limitations of the current methods.

1. **Lack of physics modeling.** Existing methods based on neural implicit representation rely solely on rendering supervision, lacking explicit incorporation of physical signals and constraints, *e.g.*, from physical simulators. This deficiency compromises their ability to optimize 3D shapes for stability.
2. **Ignorance of thin structures.** Previous methods primarily focus on optimizing substantial parts of objects within images, struggling to capture the slender structures crucial for object stability. This can be attributed to the overly-smoothed and averaged optimization results from problematic geometric priors, including multi-modal inconsistency (*e.g.*, depth-normal), multi-view inconsistency, and inaccurate predictions deviating from the true underlying 3D geometry.

To address these limitations, we present PHYRECON, a novel method representing the first effort to *integrate differentiable rendering and differentiable physical simulations for learning implicit surface representations*. Specifically, we propose a differentiable particle-based physical simulator and an efficient algorithm, Surface Points Marching Cubes (SP-MC), for differentiable transformation between SDF-based implicit representation and explicit surface points. The simulator facilitates accurate computation of 3D rigid body dynamics subjected to forces of gravity, contact, and friction. Notably, both background and foreground objects for simulation are derived from the implicit scene representation, eliminating the need for 3D scene priors. In the forward phase, the simulator delineates the physical behavior of objects, leading to a straightforward yet effective physical loss that discourages movement within the simulation. This process also generates dynamic data, such as 3D contact points, providing intricate details about the current shapes of the objects. With an efficient implementation, our differentiable pipeline optimizes the implicit surface representation by coherently integrating feedback through back-propagation from both rendering and physical losses.

Moreover, to enhance the reconstruction of intricate structures and address the geometric prior inconsistencies, we propose a joint uncertainty model for describing both the rendering and physical uncertainty. The rendering uncertainty is designed to identify and mitigate inconsistencies arising from multi-view geometric priors, while the physical uncertainty models the motion trajectory of the 3D contact points in the physical simulator, offering precise and interpretable monitoring of regions lacking physical support. Utilizing these uncertainties, we adaptively adjust the per-pixel depth, normal, and instance mask losses to avoid erroneous priors in surface reconstruction. Observing that intricate geometries that occupy fewer pixels are less likely to be sampled, we further propose a physics-guided pixel sampling based on physical uncertainty to help recover slender structures.

We conduct extensive experiments on both real datasets including ScanNet [6] and ScanNet++ [68], and synthetic dataset Replica [56]. Results on multiple metrics, *i.e.*, scene reconstruction, object reconstruction, and object stability, demonstrate that our method significantly surpasses all state-of-the-art methods in terms of both reconstruction quality and physical plausibility. Through ablative studies, we highlight the effectiveness of physical loss and uncertainty modeling in enhancing object stability and reconstruction quality. Remarkably, our approach achieves significant advancements in stability, *registering at least a 40% improvement across all examined datasets*, as assessed using the physical simulator Isaac Gym [33]. We will release the code upon paper acceptance.

In summary, we introduce PHYRECON, which facilitates efficient joint modeling with scene appearance, geometry, and physics. In summary, our main contributions are:

1. We introduce the first method that seamlessly bridges neural scene reconstruction and physics simulation through a differentiable particle-based physical simulator and the proposed SP-MC that efficiently transforms implicit representation into explicit surface points. Our method enables differentiable optimization with both rendering and physical losses.
2. We propose a novel method that jointly models the rendering and physical uncertainties. By dynamically adjusting the per-pixel rendering loss and physics-guided pixel sampling, our model largely improves the reconstruction of thin structures.
3. Extensive experiments and ablations demonstrate that our model significantly enhances reconstruction quality and physical plausibility, outperforming state-of-the-art methods. Our results exhibit substantial stability improvements in physical simulators, signaling a broader potential for physics-demanding applications.

2 Related Work

Neural Implicit Surface Reconstruction Recently, neural implicit surface representations [41, 72, 30, 44, 4, 34] have gained popularity in 3D reconstruction. Advances in implicit volume rendering (*e.g.*, Neural Radiance Fields (NeRF) [39, 73]) have spurred new efforts in surface representation learning from multi-view images. Several studies [45, 58, 67] are proposed to connect the volume density in NeRF, excelling in photo-realistic rendering, with the geometric representation of iso-surface, *e.g.*, occupancy [36, 43] or signed distance function (SDF) [47, 3]. Recent methods [60, 26, 61, 29] further achieve compositional scene reconstruction by decomposing the latent 3D scene representation into the background and foreground objects. Despite achieving plausible object disentanglement, these methods fail to yield physically plausible reconstruction results, primarily due to the absence of physics constraints in existing neural implicit reconstruction pipelines. This paper addresses this limitation by incorporating both physical and appearance cues with implicit surface representation. Bridging this gap involves a differentiable particle-based physical simulator and an efficient transformation from the SDF-based implicit representation to explicit surface points, thereby enabling surface learning with both rendering and physical losses.

Prior Regularization in Implicit Representation Learning To enhance optimization and robustness, researchers have employed various priors such as depth smoothness [9, 65, 66, 42], semantic similarity [22, 25, 7], or sparse MVS point clouds [59, 8, 50] for novel view synthesis. Regarding surface reconstruction, Guo *et al.* [18] propose Manhattan-world assumptions for the planar regions, Wang *et al.* [57] use normal priors for indoor scene reconstruction, and Yu *et al.* [69] utilizes both normal and depth predictions from off-the-shelf model [12] as priors to regularize the texture-less regions. Compositional reconstruction methods [29, 61] introduce additional geometrical priors to regularize object disentanglement and unobserved regions. However, these priors primarily involve geometry and appearance, neglecting physics priors despite their critical role in assessing object shapes and achieving stability. This paper proposes to incorporate physical priors into the neural implicit surface representation through a differentiable simulator. We introduce physical loss to penalize object movement, as well as a joint uncertainty modeling with both rendering and physical uncertainty. Rendering uncertainty filters multi-view inconsistencies in the monocular geometric priors, akin to prior work [35, 51, 46, 62]. The physical uncertainty employs the 3D contact points from the simulator to offer accurate insights into areas lacking physical support, which helps modulate the rendering losses and guides pixel sampling.

Physics in Scene Understanding There has been an increasing interest in incorporating physics commonsense in the scene understanding community, spanning various topics such as object gen-

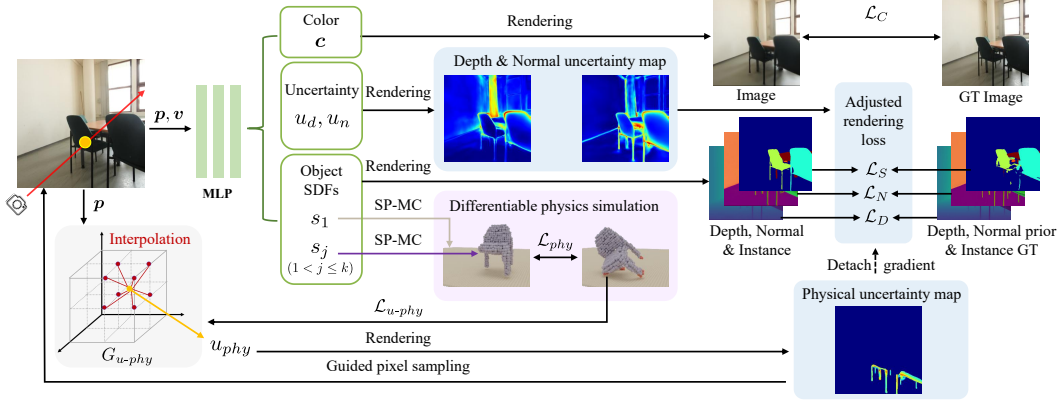


Figure 2: **Overview of PHYRECON.** We incorporate explicit physical constraints in the neural scene reconstruction through a differentiable particle-based physical simulator and a differentiable transformation (*i.e.*, SP-MC) between implicit surface function and explicit surface points. To learn intricate 3D structures, we introduce rendering and physical uncertainty to address the inconsistencies in the geometric priors and guide the pixel sampling.

eration [40, 14, 55, 38, 37], object decomposition [31, 74], material simulation [23, 28, 63], scene synthesis [48, 64], and human motion generation [49, 53, 21, 71, 70, 20, 5]. In the context of scene reconstruction, previous work primarily focus on applying collision loss at the granularity of 3D bounding boxes to adjust their translations and rotations [11, 2]. Zhang *et al.* [72] proposes to penalize the penetration between objects within the occupancy representation. In this paper, we propose to incorporate physics information into the neural implicit surface representation through a differentiable simulator, significantly enhancing both the richness of the physical information and the granularity of the optimization. The simulator not only furnishes detailed object trajectories but also yields detailed information about the object shapes in the form of 3D contact points. With physical loss directly backpropagated to the implicit shape representation, our approach leads to a refined optimization of object shapes and physical stability.

3 Method

Given an input set of N posed RGB images $\mathcal{I} = \{I_1, \dots, I_N\}$ and corresponding instance masks $\mathcal{S} = \{S_1, \dots, S_N\}$, our objective is to reconstruct each object and the background in the scene. Fig. 2 presents an overview of our proposed PHYRECON.

3.1 Neural Scene Reconstruction

Volume Rendering of SDF-based Implicit Surfaces We utilize neural implicit surfaces with SDF to represent 3D geometry for implicit reconstruction. The SDF provides a continuous function that yields the distance $s(\mathbf{p})$ to the closest surface for a given point \mathbf{p} , with the sign indicating whether the point lies inside (negative) or outside (positive) the surface. The zero-level set of the SDF function $\Omega = \{\mathbf{p} \in \mathbb{R}^3 \mid s(\mathbf{p}) = 0\}$ implicitly represents the surface. Following the previous work [69], we implement the SDF function as a multi-layer perceptron (MLP) network $f(\cdot)$, and similarly, the appearance function as another MLP network $g(\cdot)$.

For each camera ray $\mathbf{r} = (\mathbf{o}, \mathbf{v})$ with \mathbf{o} as the ray origin and \mathbf{v} as the viewing directing, n points $\{\mathbf{p}_i = \mathbf{o} + t_i \mathbf{v} \mid i = 0, 1, \dots, n-1\}$ are sampled, where t_i is the distance from the sample point to the camera center. We predict the SDF $s(\mathbf{p}_i)$ and the color \mathbf{c}_i for each point along the ray. The predicted color $\hat{\mathbf{C}}(\mathbf{r})$ for the ray \mathbf{r} is computed with the unbiased rendering method following NeuS [58] as:

$$\hat{\mathbf{C}}(\mathbf{r}) = \sum_{i=0}^{n-1} T_i \alpha_i \mathbf{c}_i, \quad (1)$$

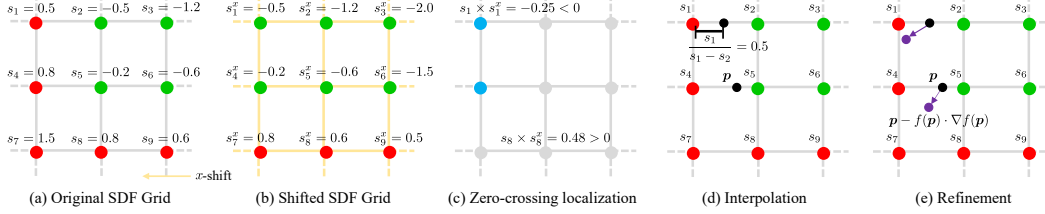


Figure 3: **Illustration of SP-MC.** Our algorithm first localizes the zero-crossing vertices \mathbf{V} (blue) through the grid-shifting operation and extracts coarse surface points $\mathbf{P}_{\text{coarse}}$ (black) through linear interpolation. Finally, the fine-grained surface points \mathbf{P}_{fine} (purple) are obtained by querying the SDF values and surface normals from the network $f(\cdot)$.

where T_i is the discrete accumulated transmittance defined by $T_i = \prod_{j=0}^{i-1} (1 - \alpha_j)$. α_i is the discrete opacity value defined as:

$$\alpha_i = \max \left(\frac{\Phi_u(s(\mathbf{p}_i)) - \Phi_u(s(\mathbf{p}_{i+1}))}{\Phi_u(s(\mathbf{p}_i))}, 0 \right), \quad (2)$$

where $\Phi_u(x) = (1 + e^{-ux})^{-1}$ and u is a learnable parameter. Similarly, we compute the depth $\hat{D}(\mathbf{r})$ and normal $\hat{\mathbf{N}}(\mathbf{r})$ of the surface intersecting the current ray \mathbf{r} as:

$$\hat{D}(\mathbf{r}) = \sum_{i=0}^{n-1} T_i \alpha_i t_i, \quad \hat{\mathbf{N}}(\mathbf{r}) = \sum_{i=0}^{n-1} T_i \alpha_i \mathbf{n}_i. \quad (3)$$

The normal of point \mathbf{p}_i is the analytical gradient of the SDF function, *i.e.*, $\mathbf{n}_i = \nabla f(\cdot)$.

Object-compositional Scene Reconstruction In this work, we consider the compositional reconstruction of k objects utilizing their corresponding masks, and we treat the background as an object for brevity [60]. More specifically, for a scene with k objects, the SDF network $f(\cdot)$ will output k SDFs at each point \mathbf{p} , and the j -th ($1 \leq j \leq k$) SDF represents the geometry of j -th object. Without loss of generality, we set $j = 1$ as the background object and others as the foreground objects. In subsequent sections of the paper, we denote the j -th object SDF at point \mathbf{p} as $s_j(\mathbf{p})$. The scene SDF $s(\mathbf{p})$ is the minimum of the object SDFs, *i.e.*, $s(\mathbf{p}) = \min s_j(\mathbf{p}), j = 1, 2, \dots, k$, which is used for sampling points along the ray and volume rendering (Eq. (2)). Moreover, each point's SDFs can be transformed into instance logits $\mathbf{h}(\mathbf{p}) = [h_1(\mathbf{p}), h_2(\mathbf{p}), \dots, h_k(\mathbf{p})]$, where

$$h_j(\mathbf{p}) = \gamma / (1 + \exp(\gamma \cdot s_j(\mathbf{p}))). \quad (4)$$

γ is a fixed parameter. Similar to Eq. (1) and Eq. (3), we can get the instance logits $\hat{\mathbf{H}}(\mathbf{r}) \in \mathbb{R}^k$ of pixel corresponds to the ray \mathbf{r} using volume rendering as:

$$\hat{\mathbf{H}}(\mathbf{r}) = \sum_{i=0}^{n-1} T_i \alpha_i \mathbf{h}_i. \quad (5)$$

3.2 Differentiable Physics Simulation in Neural Scene Reconstruction

To achieve the joint modeling of physics, geometry, and appearance, we propose a novel framework that bridges neural scene reconstruction and physics simulation. The foundational techniques include a particle-based physical simulator and a highly efficient method for transitioning from SDF-based neural implicit representations, which are adept at modeling visual appearances, to explicit representations that are conducive to physics simulation. Emphasizing efficiency, our simulator and the transformation process enhance the learning of neural implicit representations by jointly optimizing them with both rendering and physical losses.

Surface Points Marching Cubes (SP-MC) Integrating physical constraints into the learning of the SDF-based implicit representation demands highly efficient and accurate extraction of surface points. However, existing methods [13, 37] fall short of attaining a satisfactory balance between efficiency and precision. Thus we develop a novel algorithm, SP-MC, for efficient and differentiable extraction

of surface points. The algorithm is inspired by the marching cube algorithm [32] which estimates the topology (*i.e.*, the vertices and connectivity of triangles) in each cell of the volumetric grid. Since surface points are only required for simulation, we improve the operation efficiency and combine the implicit SDF network $f(\cdot)$ to create fine-grained surface points.

Fig. 3 illustrates the SP-MC algorithm. Formally, let $\mathbf{S} \in \mathbb{R}^{N \times N \times N}$ denote a discretized signed distance field obtained using $f(\cdot)$, where $\mathbf{S}(\mathbf{p}) \in \mathbb{R}$ denotes the signed distance of the vertex \mathbf{p} to its closest surface. SP-MC first locates the zero-crossing vertices \mathbf{V} , where a sign change occurs from the neighboring vertices in signed distances. This is achieved through a grid-shifting operation along the x , y , and z axis, respectively. For example, shifting along the x axis results in $\mathbf{S}^x(i, j, k) = \mathbf{S}(i + 1, j, k)$. Then each vertex $\mathbf{p} \in \mathbf{V}$ can be found through the element-wise multiplication of \mathbf{S} and the shifted grids $\mathbf{S}^{d \in \{x, y, z\}}$, together with its sign-flipping neighbor vertex denoted as $\mathbf{p}^{\text{shift}}$. Next, the locations of coarse surface points $\mathbf{P}_{\text{coarse}}$ are determined along the grid edge via linear interpolation:

$$\mathbf{P}_{\text{coarse}} = \left\{ \mathbf{p} + \frac{\mathbf{S}(\mathbf{p})}{\mathbf{S}(\mathbf{p}) - \mathbf{S}(\mathbf{p}^{\text{shift}})} (\mathbf{p}^{\text{shift}} - \mathbf{p}) \mid \mathbf{p} \in \mathbf{V} \right\}. \quad (6)$$

Finally, the fine-grained surface points are obtained from $\mathbf{P}_{\text{coarse}}$ using their surface normals and signed distances by:

$$\mathbf{P}_{\text{fine}} = \{ \mathbf{p} - f(\mathbf{p}) \cdot \nabla f(\mathbf{p}) \mid \mathbf{p} \in \mathbf{P}_{\text{coarse}} \}. \quad (7)$$

Benefiting from the shifting operation, friendly for parallel computation, our SP-MC implementation is capable of extracting object surface points faster than the Kaolin [13] algorithm from NVIDIA with less GPU memory consumption. In the meantime, it also achieves unbiased estimation of the surface points compared with direct thresholding the signed distance field [37], which is crucial for learning fine structures. For detailed algorithm and quantitative computational comparisons, please refer to the *supplementary*.

Particle-based Physical Simulator Leveraging the efficient transformation, we incorporate physics constraints into the neural implicit reconstruction by developing a fully differentiable particle-based simulator implemented with DiffTaichi [19]. Our simulator is designed for realistic simulations between one object and the background under the influence of gravity, friction, and contact forces. We utilize this simulator to track the motion trajectory of the object’s surface points \mathbf{P}_{fine} until reaching stability or a maximum simulation step size. The initial position of each point \mathbf{p} is denoted as \mathbf{p}^0 and the final position as $\mathbf{p}^{\text{final}}$. The simulator additionally records the point set that contacts with the floor during the simulation, denoted as $\mathbf{P}_{\text{contact}} \subset \mathbf{P}_{\text{fine}}$. For more implementation details, please refer to the *supplementary*.

Utilizing the final state of the object points and the contact points from the simulator, we present our simple yet effective physical loss:

$$\mathcal{L}_{\text{phy}} = \sum_{\mathbf{p} \in \mathbf{P}_{\text{contact}}} \|\mathbf{p}^{\text{final}} - \mathbf{p}^0\|_2, \quad (8)$$

which intuitively penalizes the movement of the object in the simulator. Note that our physical loss is only applied to the 3D contact points $\mathbf{P}_{\text{contact}}$ instead of all the surface points. If the physical loss is homogeneously applied to all the surface points, it will lead to degenerated results, contradicting the rendering cues when the object is unstable. The contact points $\mathbf{P}_{\text{contact}}$, on the other hand, are the most crucial indicators for the object stability. As shown in the experiment section, our design leads to stable 3D geometry under the coordination between the appearance and physics constraints.

3.3 Joint Uncertainty Modeling

Apart from the absence of explicit physical constraints, another important factor that hinders 3D object stability is the missing of thin structures in the reconstruction. This is largely attributed to the inconsistent results of the geometric priors from the existing monocular prediction models. Therefore, we propose a joint uncertainty modeling approach, encompassing both rendering and physical uncertainty, to mitigate the inconsistencies and improve the reconstruction of thin structures.

Rendering Uncertainty The rendering uncertainty is designed to address the issue of multi-view and multi-modal inconsistencies in monocular geometry priors, including depth uncertainty and

normal uncertainty. We model the depth uncertainty u_d and normal uncertainty u_n of a 3D point as view-dependent representations [46, 52, 62], which we utilize the appearance network $g(\cdot)$ to predict along with the color c for a 3D point \mathbf{p} :

$$g : (\mathbf{p} \in \mathbb{R}^3, \mathbf{n} \in \mathbb{R}^3, \mathbf{v} \in \mathbb{R}^3, \mathbf{f} \in \mathbb{R}^{256}) \mapsto (c \in \mathbb{R}^3, u_d \in \mathbb{R}, u_n \in \mathbb{R}). \quad (9)$$

\mathbf{n} is the normal at \mathbf{p} , \mathbf{v} is the viewing direction, \mathbf{f} is a geometry latent feature output from the SDF network $f(\cdot)$. Then we can compute the depth uncertainty $\hat{U}_d(\mathbf{r})$ and normal uncertainty $\hat{U}_n(\mathbf{r})$ of a pixel corresponds to the ray \mathbf{r} through volume rendering:

$$\hat{U}_d(\mathbf{r}) = \sum_{i=0}^{n-1} T_i \alpha_i u_{d,i}, \quad \hat{U}_n(\mathbf{r}) = \sum_{i=0}^{n-1} T_i \alpha_i u_{n,i}. \quad (10)$$

Subsequently, we can modulate the L_2 depth loss $\mathcal{L}_D(\mathbf{r})$ and L_1 normal loss $\mathcal{L}_N(\mathbf{r})$ based on the rendering uncertainty:

$$\mathcal{L}_{D_U}(\mathbf{r}) = \ln(|\hat{U}_d(\mathbf{r})| + 1) + \frac{\mathcal{L}_D(\mathbf{r})}{|\hat{U}_d(\mathbf{r})|}, \quad \mathcal{L}_{N_U}(\mathbf{r}) = \ln(|\hat{U}_n(\mathbf{r})| + 1) + \frac{\mathcal{L}_N(\mathbf{r})}{|\hat{U}_n(\mathbf{r})|}. \quad (11)$$

Intuitively, the uncertainty-aware rendering loss can assign higher uncertainty to the pixels with larger loss, thus filtering the negative impact from the inconsistent monocular priors when the prediction from one viewpoint differs from other views. Note that although depth uncertainty and normal uncertainty are not directly supervised, they are automatically optimized through multi-view rendering coordination. Fig. 6 shows visualizations of the rendered uncertainty maps, where the inconsistent monocular priors are precisely localized by higher uncertainty.

Physical Uncertainty Apart from the rendering uncertainty, we introduce physical uncertainty, which directly utilizes information from the physical simulator, offering accurate and interpretable insights into the areas that lack physical support. More specifically, we represent the physical uncertainty field for the scene by a dense grid $G_{u\text{-phy}} \in \mathbb{R}^{N \times N \times N}$. The physical uncertainty $u_{\text{phy}}(\mathbf{p}) \in \mathbb{R}$ for a 3D point \mathbf{p} is obtained through trilinear interpolation:

$$u_{\text{phy}}(\mathbf{p}) = \text{Interp}(G_{u\text{-phy}}, \mathbf{p}). \quad (12)$$

$G_{u\text{-phy}}$ is initialized to zero and then updated after each physics simulation using the 3D contact points $\mathbf{P}_{\text{contact}}$ from the simulator. Specifically, for each contact point $\mathbf{p} \in \mathbf{P}_{\text{contact}}$, we track its trajectory by interpolating from its initial position to its first contact position with the ground. The interpolated points of all contact points form the uncertain point set in one simulation trial, denoted by \mathbf{P}_u . We design a loss function $\mathcal{L}_{u\text{-phy}}$ to update $G_{u\text{-phy}}$ through backpropagation:

$$\mathcal{L}_{u\text{-phy}} = -\xi \sum_{\mathbf{p} \in \mathbf{P}_u} u_{\text{phy}}(\mathbf{p}), \quad (13)$$

where $\xi > 0$ represents the increasing rate for $G_{u\text{-phy}}$. As a result, areas with high physical uncertainty values indicate that the object lacks support and requires the development of supporting structures. The physical uncertainty $\hat{U}_{\text{phy}}(\mathbf{r})$ of pixel corresponds to the ray \mathbf{r} is computed by volume rendering:

$$\hat{U}_{\text{phy}}(\mathbf{r}) = \sum_{i=0}^{n-1} T_i \alpha_i u_{\text{phy},i}. \quad (14)$$

Finally, we present the depth, normal and instance semantic loss re-weighted by both rendering and physical uncertainty:

$$\begin{aligned} \mathcal{L}_D &= \sum_{\mathbf{r} \in \mathcal{R}} \frac{1}{\hat{U}_{\text{phy}}(\mathbf{r}) + 1} \mathcal{L}_D(\mathbf{r}), \\ \mathcal{L}_N &= \sum_{\mathbf{r} \in \mathcal{R}} \frac{1}{\hat{U}_{\text{phy}}(\mathbf{r}) + 1} \mathcal{L}_N(\mathbf{r}), \\ \mathcal{L}_S &= \sum_{\mathbf{r} \in \mathcal{R}} \frac{1}{\hat{U}_{\text{phy}}(\mathbf{r}) + 1} \mathcal{L}_S(\mathbf{r}). \end{aligned} \quad (15)$$

The cross-entropy segmentation loss $\mathcal{L}_S(\mathbf{r})$ is weighted only by the physical uncertainty since we use view-consistent instance masks \mathcal{S} following prior work [29, 61] on compositional scene reconstruction. Note that we detach $\hat{U}_{\text{phy}}(\mathbf{r})$ in the above formulations. Thus, the physical uncertainty field $G_{u\text{-phy}}$ will only reflect the accurate physical information from the simulator. Visualizations of the physical uncertainty are in Fig. 6.

Physics-Guided Pixel Sampling Another critical observation in indoor scene reconstruction is that intricate object structures take up only a minor portion of the image, leading to a lower possibility of being sampled despite its significance in preserving object stability. How to effectively pinpoint the fine and detailed geometries, typically associated with high-frequency surfaces, is a perceptually challenging task. On the other hand, physical uncertainty precisely outlines the areas where the object lacks support and thus requires special attention for optimization. Hence, we introduce a physics-guided pixel sampling strategy to enhance the learning of detailed 3D structures. With physical uncertainty, we calculate the sampling probability of each pixel in the entire image by:

$$p(\mathbf{r}) = \frac{\hat{U}_{phy}(\mathbf{r})}{\sum_{\mathbf{r} \in \mathcal{R}} \hat{U}_{phy}(\mathbf{r})} \quad (16)$$

3.4 Training Details

In summary, our overall loss function is:

$$\mathcal{L} = \mathcal{L}_{RGB} + \mathcal{L}_D + \mathcal{L}_N + \mathcal{L}_S + \mathcal{L}_{phy} + \mathcal{L}_{u-phy} + \mathcal{L}_{reg}, \quad (17)$$

where the loss weights are omitted for simplicity. Following prior work [16, 69, 29], we introduce \mathcal{L}_{reg} to regularize the unobservable regions for background and foreground objects, as well as the implicit shapes through an eikonal term.

To ensure robust optimization and coordination among various components, we empirically divide the training into three stages. In the first stage, we exclusively leverage the rendering losses with rendering uncertainties. In the second stage, we introduce our physical simulator to incorporate physical uncertainty into rendering losses and enable physics-guided pixel sampling. Finally, we integrate the physical loss using a learning curriculum that gradually increases the physical loss weight. The staged training allows the simulator to pinpoint more accurate contact points, essential for effective optimization of shape through the physical loss. For further details about the loss, training, and implementation details, please refer to *supplementary*.

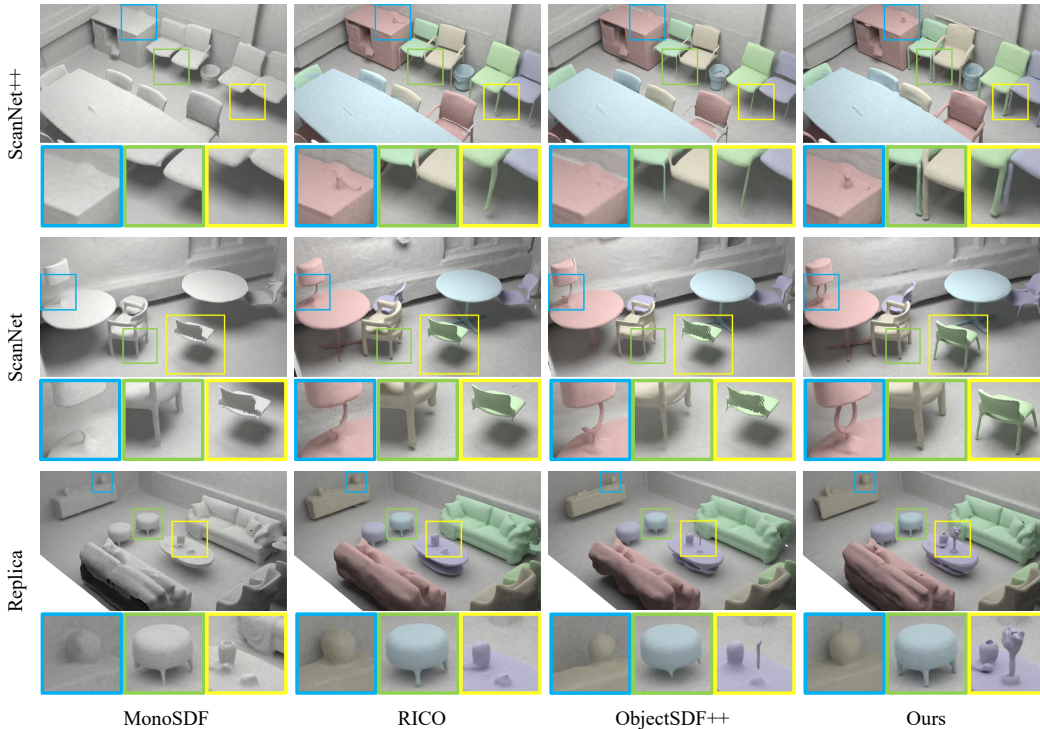


Figure 4: **Qualitative results of indoor scene reconstruction.** Examples from ScanNet++ [68], ScanNet [6] and Replica [56] demonstrate our model produces higher quality reconstructions compared with the baselines. Our results contain finer details for slender structures (chair legs and the objects on the table) and plausible support relations, which are shown in the zoom-in boxes.

4 Experiments

We assess the effectiveness of PHYRECON by evaluating scene and object reconstruction quality, as well as object stability, in comparison to state-of-the-art methods. Additionally, we conducted extensive ablation experiments to verify the power of each component of our approach. We present failure cases and a discussion of limitations in *supplementary*.

4.1 Settings

Datasets We conduct experiments on both the synthetic dataset Replica [56] and real datasets ScanNet [6] and ScanNet++ [68]. Replica is a synthesized dataset with accurate camera poses and clear object masks. Following previous settings [69, 61], we use the same test split of 8 scenes in our experiments. ScanNet is a real-world dataset, captured with an RGB-D camera with 2D instance segmentation masks alongside RGB images as annotations. We use the test split from Li *et al.* [29] to test on 7 scenes. Additionally, we conduct experiments on another 7 scenes from the recently proposed real-world dataset ScanNet++, which offers higher-quality images and more accurate camera poses. Data preparation details, including monocular cues and GT instance mask generation, are in *supplementary*.

Metrics For reconstruction, we measure the Chamfer Distance (CD) in *cm*, the F-score (F-score) with a threshold of *5cm*, as well as Normal Consistency (NC). These metrics are evaluated for both scene and object reconstruction across all datasets. Due to the imperfect 3D ground truth on ScanNet and ScanNet++, we follow Yu *et al.* [18, 69] to evaluate reconstruction only on the visible areas. To evaluate the physical plausibility of the reconstructed objects, we report the Stability Ratio (SR), which is defined as the ratio of the number of physically stable objects against the total number of objects in the scene. The physical stability is defined as being within certain thresholds in both object rotation and translation after the simulation. The assessment is conducted using dropping simulation via the Isaac Gym simulator [33] to avoid bias in favor of our method. We provide more details on our evaluation procedure in *supplementary*.

Baselines We choose MonoSDF [69], RICO [29] and ObjectSDF++ [61] as the baseline models. MonoSDF employs geometric cues to reconstruct the whole scene whereas RICO and ObjectSDF++ further use neural implicit representation for object-compositional surface reconstruction. Thus we only evaluate the quality of scene reconstruction on MonoSDF.

Table 1: **Quantitative Results of 3D Reconstruction.** Results on ScanNet++ [68], ScanNet [6] and Replica [56] datasets demonstrate our model reaches the best reconstruction quality and significantly improves on physical stability.

Dataset	Method	Scene Recon.			Obj. Recon.			Obj. Stability
		CD↓	F-Score↑	NC↑	CD↓	F-score↑	NC↑	SR (%) ↑
ScanNet++	MonoSDF	3.94	78.14	89.37	-	-	-	-
	RICO	3.87	78.45	89.64	4.29	85.91	85.45	26.43
	ObjectSDF++	3.79	79.12	89.57	4.08	86.32	85.32	25.28
	Ours	3.34	81.53	90.10	3.28	87.21	86.16	78.16
ScanNet	MonoSDF	8.97	60.30	84.40	-	-	-	-
	RICO	8.92	61.44	84.58	9.29	73.10	79.44	29.68
	ObjectSDF++	8.86	61.68	85.20	9.21	74.82	81.05	26.56
	Ours	8.34	63.01	86.57	7.92	75.54	82.54	70.31
Replica	MonoSDF	3.87	85.01	88.59	-	-	-	-
	RICO	3.86	84.66	88.68	4.16	80.38	84.30	32.89
	ObjectSDF++	3.73	85.50	88.60	3.99	80.71	84.22	30.26
	Ours	3.68	85.61	89.45	3.86	81.30	84.91	77.63

4.2 Results

Tab. 1 and Fig. 4 present the quantitative and qualitative results of the neural scene reconstruction. In Fig. 5, we visualize the trajectory for the reconstructed object during dropping simulation in Isaac

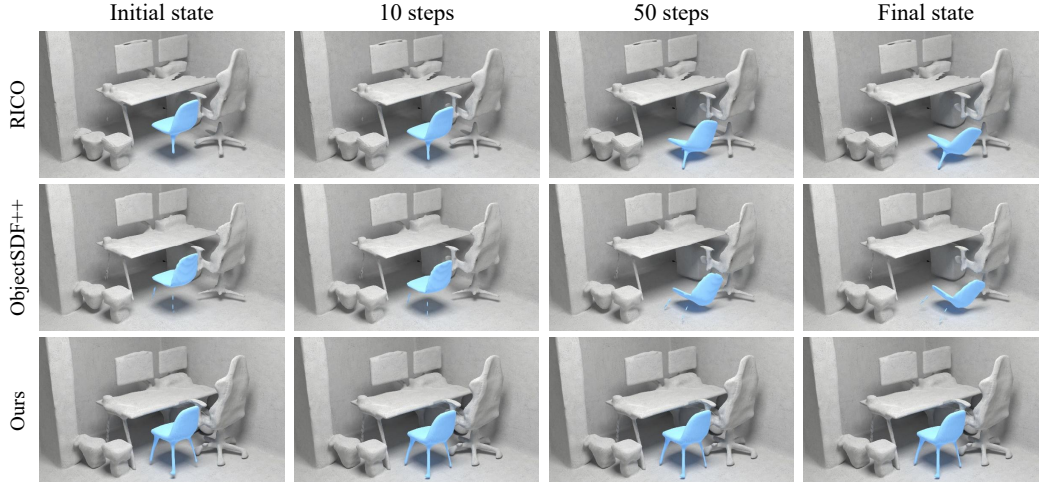


Figure 5: **Object trajectory during simulation.** Our method enhances the physical plausibility of the reconstruction results, which can remain stable during dropping simulation in Isaac Gym.

Gym [33]. Fig. 6 showcases visualizations of several critical components in our methods, including the sampling strategy, volume renderings of the geometric cues, and the uncertainty maps. Our method significantly outperforms all baselines, and we summarize the observations from several aspects as follows.

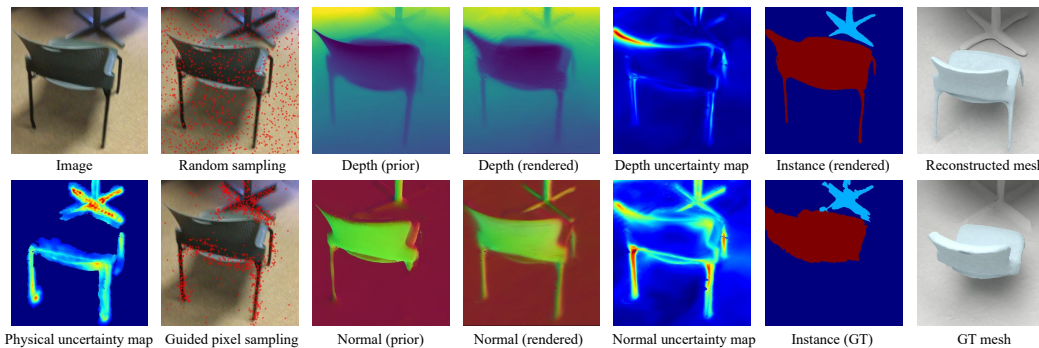


Figure 6: **Joint uncertainty modeling.** The physical uncertainty pinpoints the regions critical for stability, efficiently guiding the pixel sampling. The rendering uncertainties can alleviate the impact of inconsistent geometry cues, leading to a better-reconstructed mesh than the GT.

Physical Stability From the quantitative results in Tab. 1, our method realizes significant improvements in object stability, outperforming all other baselines by at least 40% across all datasets. This signifies *a significant stride towards achieving physically plausible scene reconstruction* from multi-view images, thereby validating the efficacy of PHYRECON in incorporating differentiable physics simulation into the neural implicit reconstruction pipeline. The notable stability improvement is attributed to two essential factors: 1) enhanced learning of intricate structures, facilitated by joint uncertainty modeling and physics-guided pixel sampling. Results from RICO [29] and ObjectSDF++ [61] in Fig. 5 fail to capture all the chair legs, leading to inherent instability, and 2) the integration of physical loss and physical uncertainty ensures the reconstructed structure closely aligns with the ground floor, as evident in the examples from Fig. 4 and Fig. 5.

Reconstruction Quality Note that the improvement of the physical plausibility does not come under the sacrifice of reconstruction quality. From the results in Tab. 1, our method surpasses all the state-of-the-art methods across three datasets in all the reconstruction metrics. As also shown in Fig. 4, while the baseline methods are capable of reconstructing substantial parts of objects, *e.g.*, sofa or table top, they struggle with the intricate structures of objects. Moreover, our model achieves much more detailed reconstruction, *e.g.*, the vase and lamp on the tables, shown in the zoom-in views.

Joint Uncertainty Modeling Furthermore, we discuss the intermediate results of our joint uncertainty modeling exemplified on the ScanNet dataset. As shown in Fig. 6, the physical uncertainty adeptly pinpoints the regions critical for remaining stability, such as the chair legs and table base. The physics-guided pixel sampling, informed by the physical uncertainty map, prioritizes intricate structures over the random sampling strategy. Moreover, it modulates rendering losses, particularly useful for instance mask loss where chair legs are absent in the ground-truth mask. Meanwhile, the depth and normal uncertainty maps identify inconsistencies in the geometric prior, *e.g.*, miss detections in the normal prior and the overly sharp depth prior. Collectively, they contribute to the physically plausible and detailed reconstructed mesh, surpassing the ground truth.

Table 2: **Ablation Results on ScanNet++ dataset.**

<i>RU</i>	<i>PU</i>	<i>PS</i>	<i>PL</i>	Scene Recon.			Obj. Recon.			Obj. Stability
				CD↓	F-Score↑	NC↑	CD↓	F-score↑	NC↑	SR (%) ↑
×	×	×	×	3.82	78.64	89.52	4.13	86.26	85.42	25.28
×	×	×	✓	3.68	79.35	89.55	3.97	86.35	85.26	68.96
✓	×	×	×	3.46	80.73	89.63	3.65	86.83	85.53	47.12
✓	✓	×	×	3.42	80.68	89.67	3.46	86.97	85.45	56.32
✓	✓	✓	×	3.31	81.64	89.94	3.34	87.17	85.47	60.91
✓	✓	✓	✓	3.34	81.53	90.10	3.28	87.21	86.16	78.16

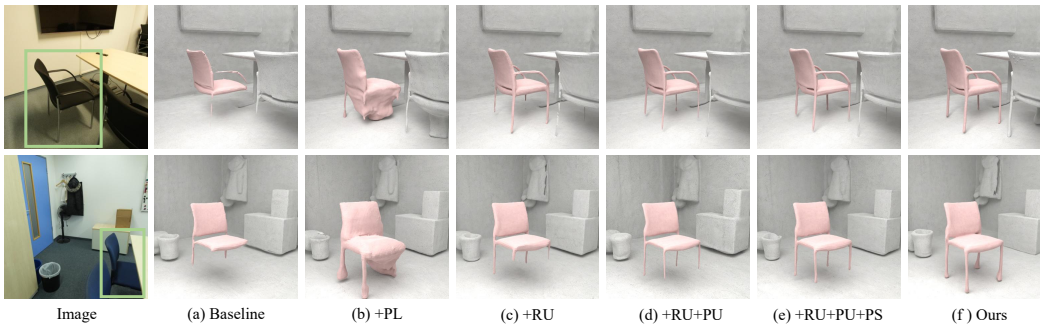


Figure 7: **Visual comparisons for ablation study.** *PL* denotes physical loss, *RU* for rendering uncertainty, *PU* for physical uncertainty and *PS* for physics-guided sampling.

4.3 Ablation Study

To analyze component effects, we conduct ablative studies on the physical loss (*PL*), rendering uncertainty (*RU*), physical uncertainty (*PU*), and physics-guided pixel sampling (*PS*). Tab. 2 and Fig. 7 illustrate quantitative and qualitative comparisons, respectively. Key findings are as follows:

1. Physical loss significantly improves the object stability for the reconstruction. However, due to the insufficient regularization of thin structures and the imprecise contact points in the simulator, adding the physical loss alone will overshadow the rendering losses, leading to degenerated object shapes to sustain stability.
2. Rendering uncertainty, physical uncertainty, and physic-guided pixel sampling collectively contribute to enhancing the reconstruction quality, particularly on thin structures. Despite the advancements, the reconstructed results still struggle to avoid physical implausibility without direct physical loss in the optimization.
3. When all components are introduced, the enhanced reconstruction of thin structures through the joint uncertainty modeling leads to more accurate contact points for the simulation. The joint optimization with physical loss not only enhances the stability of objects but also preserves their reasonable shapes, leading to neural scene reconstruction with both physical plausibility and fine details simultaneously.

5 Conclusion

In conclusion, this paper introduces PHYRECON as the first approach to leverage both differentiable rendering and differentiable physics simulation for learning implicit surface representations. Our framework features a novel differentiable particle-based physical simulator and joint uncertainty modeling, facilitating efficient optimization with both rendering and physical losses. Extensive experiments validate the effectiveness of PHYRECON, showcasing its significant outperformance of all state-of-the-art methods in terms of both reconstruction quality and physics stability, underscoring its potential for future physics-demanding applications.

References

- [1] Anderson, P., Wu, Q., Teney, D., Bruce, J., Johnson, M., Sünderhauf, N., Reid, I., Gould, S., Van Den Hengel, A.: Vision-and-language navigation: Interpreting visually-grounded navigation instructions in real environments. In: Conference on Computer Vision and Pattern Recognition (CVPR) (2018)
- [2] Chen, Y., Huang, S., Yuan, T., Zhu, Y., Qi, S., Zhu, S.: Holistic++ scene understanding: Single-view 3d holistic scene parsing and human pose estimation with human-object interaction and physical commonsense. In: International Conference on Computer Vision (ICCV) (2019)
- [3] Chen, Y., Ni, J., Jiang, N., Zhang, Y., Zhu, Y., Huang, S.: Single-view 3d scene reconstruction with high-fidelity shape and texture. In: International Conference on 3D Vision (3DV) (2024)
- [4] Chibane, J., Alldieck, T., Pons-Moll, G.: Implicit functions in feature space for 3d shape reconstruction and completion. In: Conference on Computer Vision and Pattern Recognition (CVPR) (2020)
- [5] Cui, J., Liu, T., Liu, N., Yang, Y., Zhu, Y., Huang, S.: Anyskill: Learning open-vocabulary physical skill for interactive agents. In: Conference on Computer Vision and Pattern Recognition (CVPR) (2024)
- [6] Dai, A., Chang, A.X., Savva, M., Halber, M., Funkhouser, T., Nießner, M.: Scannet: Richly-annotated 3d reconstructions of indoor scenes. In: Conference on Computer Vision and Pattern Recognition (CVPR) (2017)
- [7] Deng, C., Jiang, C., Qi, C.R., Yan, X., Zhou, Y., Guibas, L., Anguelov, D., et al.: Nerdi: Single-view nerf synthesis with language-guided diffusion as general image priors. In: Conference on Computer Vision and Pattern Recognition (CVPR). pp. 20637–20647 (2023)
- [8] Deng, K., Liu, A., Zhu, J.Y., Ramanan, D.: Depth-supervised NeRF: Fewer views and faster training for free. In: Conference on Computer Vision and Pattern Recognition (CVPR) (2022)
- [9] Donne, S., Geiger, A.: Learning non-volumetric depth fusion using successive reprojections. In: Conference on Computer Vision and Pattern Recognition (CVPR). pp. 7634–7643 (2019)
- [10] Drebin, R.A., Carpenter, L., Hanrahan, P.: Volume rendering. *ACM Siggraph Computer Graphics* **22**(4), 65–74 (1988)
- [11] Du, Y., Liu, Z., Basevi, H., Leonardis, A., Freeman, W.T., Tenenbaum, J.T., Wu, J.: Learning to exploit stability for 3d scene parsing. In: Advances in Neural Information Processing Systems (NeurIPS) (2018)
- [12] Eftekhari, A., Sax, A., Malik, J., Zamir, A.: Omnidata: A scalable pipeline for making multi-task mid-level vision datasets from 3d scans. In: International Conference on Computer Vision (ICCV) (2021)
- [13] Fuji Tsang, C., Shugrina, M., Lafleche, J.F., Takikawa, T., Wang, J., Loop, C., Chen, W., Jatavallabhula, K.M., Smith, E., Rozantsev, A., Perel, O., Shen, T., Gao, J., Fidler, S., State, G., Gorski, J., Xiang, T., Li, J., Li, M., Lebedev, R.: Kaolin: A pytorch library for accelerating 3d deep learning research. <https://github.com/NVIDIAGameWorks/kaolin> (2022)

- [14] Gao, L., Yang, J., Wu, T., Yuan, Y.J., Fu, H., Lai, Y.K., Zhang, H.: Sdm-net: Deep generative network for structured deformable mesh. *ACM Transactions on Graphics (TOG)* (2019)
- [15] Gong, R., Huang, J., Zhao, Y., Geng, H., Gao, X., Wu, Q., Ai, W., Zhou, Z., Terzopoulos, D., Zhu, S.C., et al.: Arnold: A benchmark for language-grounded task learning with continuous states in realistic 3d scenes. *arXiv preprint arXiv:2304.04321* (2023)
- [16] Gropp, A., Yariv, L., Haim, N., Atzmon, M., Lipman, Y.: Implicit geometric regularization for learning shapes. In: *International Conference on Machine Learning (ICML)* (2020)
- [17] Gu, J., Xiang, F., Li, X., Ling, Z., Liu, X., Mu, T., Tang, Y., Tao, S., Wei, X., Yao, Y., et al.: Maniskill2: A unified benchmark for generalizable manipulation skills. *arXiv preprint arXiv:2302.04659* (2023)
- [18] Guo, H., Peng, S., Lin, H., Wang, Q., Zhang, G., Bao, H., Zhou, X.: Neural 3d scene reconstruction with the manhattan-world assumption. In: *Conference on Computer Vision and Pattern Recognition (CVPR)* (2022)
- [19] Hu, Y., Anderson, L., Li, T.M., Sun, Q., Carr, N., Ragan-Kelley, J., Durand, F.: DiffTaichi: Differentiable programming for physical simulation. In: *International Conference on Learning Representations (ICLR)* (2020)
- [20] Huang, S., Wang, Z., Li, P., Jia, B., Liu, T., Zhu, Y., Liang, W., Zhu, S.C.: Diffusion-based generation, optimization, and planning in 3d scenes. In: *Conference on Computer Vision and Pattern Recognition (CVPR)* (2023)
- [21] Isogawa, M., Yuan, Y., O’Toole, M., Kitani, K.M.: Optical non-line-of-sight physics-based 3d human pose estimation. In: *Conference on Computer Vision and Pattern Recognition (CVPR)*. pp. 7013–7022 (2020)
- [22] Jain, A., Tancik, M., Abbeel, P.: Putting nerf on a diet: Semantically consistent few-shot view synthesis. In: *International Conference on Computer Vision (ICCV)* (2021)
- [23] Jiang, C., Schroeder, C., Selle, A., Teran, J., Stomakhin, A.: The affine particle-in-cell method. *ACM Transactions on Graphics (TOG)* **34**(4), 1–10 (2015)
- [24] Jiang, Y., Gupta, A., Zhang, Z., Wang, G., Dou, Y., Chen, Y., Fei-Fei, L., Anandkumar, A., Zhu, Y., Fan, L.: Vima: General robot manipulation with multimodal prompts. *arXiv* (2022)
- [25] Kim, M., Seo, S., Han, B.: Infonerf: Ray entropy minimization for few-shot neural volume rendering. In: *Conference on Computer Vision and Pattern Recognition (CVPR)*. pp. 12912–12921 (2022)
- [26] Kong, X., Liu, S., Taher, M., Davison, A.J.: vmap: Vectorised object mapping for neural field slam. In: *Proceedings of the IEEE/CVF Conference on Computer Vision and Pattern Recognition*. pp. 952–961 (2023)
- [27] Krantz, J., Wijmans, E., Majumdar, A., Batra, D., Lee, S.: Beyond the nav-graph: Vision-and-language navigation in continuous environments. In: *European Conference on Computer Vision (ECCV)* (2020)
- [28] Li, X., Qiao, Y.L., Chen, P.Y., Jatavallabhula, K.M., Lin, M., Jiang, C., Gan, C.: Pac-nerf: Physics augmented continuum neural radiance fields for geometry-agnostic system identification. In: *International Conference on Learning Representations (ICLR)* (2023)
- [29] Li, Z., Lyu, X., Ding, Y., Wang, M., Liao, Y., Liu, Y.: Rico: Regularizing the unobservable for indoor compositional reconstruction. In: *International Conference on Computer Vision (ICCV)* (2023)
- [30] Liu, H., Zheng, Y., Chen, G., Cui, S., Han, X.: Towards high-fidelity single-view holistic reconstruction of indoor scenes. In: *European Conference on Computer Vision (ECCV)* (2022)
- [31] Liu, Z., Freeman, W.T., Tenenbaum, J.B., Wu, J.: Physical primitive decomposition. In: *European Conference on Computer Vision (ECCV)* (2018)

- [32] Lorensen, W.E., Cline, H.E.: Marching cubes: A high resolution 3d surface construction algorithm. *ACM Transactions on Graphics (TOG)* (1987)
- [33] Makoviychuk, V., Wawrzyniak, L., Guo, Y., Lu, M., Storey, K., Macklin, M., Hoeller, D., Rudin, N., Allshire, A., Handa, A., State, G.: Isaac gym: High performance gpu-based physics simulation for robot learning (2021)
- [34] Martel, J.N., Lindell, D.B., Lin, C.Z., Chan, E.R., Monteiro, M., Wetzstein, G.: Acorn: Adaptive coordinate networks for neural scene representation. *arXiv preprint arXiv:2105.02788* (2021)
- [35] Martin-Brualla, R., Radwan, N., Sajjadi, M.S.M., Barron, J.T., Dosovitskiy, A., Duckworth, D.: Nerf in the wild: Neural radiance fields for unconstrained photo collections. In: *Conference on Computer Vision and Pattern Recognition (CVPR)* (2021)
- [36] Mescheder, L., Oechsle, M., Niemeyer, M., Nowozin, S., Geiger, A.: Occupancy networks: Learning 3d reconstruction in function space. In: *Conference on Computer Vision and Pattern Recognition (CVPR)* (2019)
- [37] Mezghanni, M., Bodrito, T., Boulkenafed, M., Ovsjanikov, M.: Physical simulation layer for accurate 3d modeling. In: *Conference on Computer Vision and Pattern Recognition (CVPR)* (2022)
- [38] Mezghanni, M., Boulkenafed, M., Lieutier, A., Ovsjanikov, M.: Physically-aware generative network for 3d shape modeling. In: *Conference on Computer Vision and Pattern Recognition (CVPR)* (2021)
- [39] Mildenhall, B., Srinivasan, P.P., Tancik, M., Barron, J.T., Ramamoorthi, R., Ng, R.: Nerf: Representing scenes as neural radiance fields for view synthesis. In: *European Conference on Computer Vision (ECCV)* (2020)
- [40] Mo, K., Guerrero, P., Yi, L., Su, H., Wonka, P., Mitra, N., Guibas, L.J.: Structurenet: Hierarchical graph networks for 3d shape generation. *arXiv preprint arXiv:1908.00575* (2019)
- [41] Nie, Y., Han, X., Guo, S., Zheng, Y., Chang, J., Zhang, J.J.: Total3dunderstanding: Joint layout, object pose and mesh reconstruction for indoor scenes from a single image. In: *Conference on Computer Vision and Pattern Recognition (CVPR)* (2020)
- [42] Niemeyer, M., Barron, J.T., Mildenhall, B., Sajjadi, M.S.M., Geiger, A., Radwan, N.: Regnerf: Regularizing neural radiance fields for view synthesis from sparse inputs. In: *Conference on Computer Vision and Pattern Recognition (CVPR)* (2022)
- [43] Niemeyer, M., Mescheder, L., Oechsle, M., Geiger, A.: Occupancy flow: 4d reconstruction by learning particle dynamics. In: *International Conference on Computer Vision (ICCV)* (2019)
- [44] Niemeyer, M., Mescheder, L., Oechsle, M., Geiger, A.: Differentiable volumetric rendering: Learning implicit 3d representations without 3d supervision. In: *Conference on Computer Vision and Pattern Recognition (CVPR)* (2020)
- [45] Oechsle, M., Peng, S., Geiger, A.: Unisurf: Unifying neural implicit surfaces and radiance fields for multi-view reconstruction. In: *International Conference on Computer Vision (ICCV)* (2021)
- [46] Pan, X., Lai, Z., Song, S., Huang, G.: Activenerf: Learning where to see with uncertainty estimation. In: *European Conference on Computer Vision (ECCV)* (2022)
- [47] Park, J.J., Florence, P., Straub, J., Newcombe, R., Lovegrove, S.: Deepsdf: Learning continuous signed distance functions for shape representation. In: *Conference on Computer Vision and Pattern Recognition (CVPR)* (2019)
- [48] Qi, S., Zhu, Y., Huang, S., Jiang, C., Zhu, S.C.: Human-centric indoor scene synthesis using stochastic grammar. In: *Conference on Computer Vision and Pattern Recognition (CVPR)* (2018)
- [49] Rempe, D., Guibas, L.J., Hertzmann, A., Russell, B., Villegas, R., Yang, J.: Contact and human dynamics from monocular video. In: *Computer Vision–ECCV 2020: 16th European Conference, Glasgow, UK, August 23–28, 2020, Proceedings, Part V* 16. pp. 71–87. Springer (2020)

- [50] Roessle, B., Barron, J.T., Mildenhall, B., Srinivasan, P.P., Nießner, M.: Dense depth priors for neural radiance fields from sparse input views. In: Conference on Computer Vision and Pattern Recognition (CVPR) (2022)
- [51] Shen, J., Ruiz, A., Agudo, A., Moreno-Noguer, F.: Stochastic neural radiance fields: Quantifying uncertainty in implicit 3d representations. In: International Conference on 3D Vision (3DV) (2021)
- [52] Shen, J., Agudo, A., Moreno-Noguer, F., Ruiz, A.: Conditional-flow nerf: Accurate 3d modelling with reliable uncertainty quantification. In: European Conference on Computer Vision (ECCV) (2022)
- [53] Shimada, S., Golyanik, V., Xu, W., Pérez, P., Theobalt, C.: Neural monocular 3d human motion capture with physical awareness. *ACM Transactions on Graphics (ToG)* **40**(4), 1–15 (2021)
- [54] Shridhar, M., Manuelli, L., Fox, D.: Cliport: What and where pathways for robotic manipulation. In: Conference on Robot Learning. pp. 894–906. PMLR (2022)
- [55] Shu, D., Cunningham, J., Stump, G., Miller, S.W., Yukish, M.A., Simpson, T.W., Tucker, C.S.: 3d design using generative adversarial networks and physics-based validation. *Journal of Mechanical Design* **142**(7), 071701 (2020)
- [56] Straub, J., Whelan, T., Ma, L., Chen, Y., Wijmans, E., Green, S., Engel, J.J., Mur-Artal, R., Ren, C., Verma, S., Clarkson, A., Yan, M., Budge, B., Yan, Y., Pan, X., Yon, J., Zou, Y., Leon, K., Carter, N., Briales, J., Gillingham, T., Mueggler, E., Pesqueira, L., Savva, M., Batra, D., Strasdat, H.M., Nardi, R.D., Goesele, M., Lovegrove, S., Newcombe, R.: The Replica dataset: A digital replica of indoor spaces. arXiv preprint arXiv:1906.05797 (2019)
- [57] Wang, J., Wang, P., Long, X., Theobalt, C., Komura, T., Liu, L., Wang, W.: Neuris: Neural reconstruction of indoor scenes using normal priors. In: European Conference on Computer Vision (ECCV) (2022)
- [58] Wang, P., Liu, L., Liu, Y., Theobalt, C., Komura, T., Wang, W.: Neus: Learning neural implicit surfaces by volume rendering for multi-view reconstruction. In: Advances in Neural Information Processing Systems (NeurIPS) (2021)
- [59] Wei, Y., Liu, S., Rao, Y., Zhao, W., Lu, J., Zhou, J.: Nerfingmvs: Guided optimization of neural radiance fields for indoor multi-view stereo. In: International Conference on Computer Vision (ICCV) (2021)
- [60] Wu, Q., Liu, X., Chen, Y., Li, K., Zheng, C., Cai, J., Zheng, J.: Object-compositional neural implicit surfaces. In: European Conference on Computer Vision (ECCV) (2022)
- [61] Wu, Q., Wang, K., Li, K., Zheng, J., Cai, J.: Objectsdf++: Improved object-compositional neural implicit surfaces. In: International Conference on Computer Vision (ICCV) (2023)
- [62] Xiao, Y., Xu, J., Yu, Z., Gao, S.: Debsdf: Delving into the details and bias of neural indoor scene reconstruction. arXiv preprint arXiv:2308.15536 (2023)
- [63] Xie, T., Zong, Z., Qiu, Y., Li, X., Feng, Y., Yang, Y., Jiang, C.: Physgaussian: Physics-integrated 3d gaussians for generative dynamics. arXiv preprint arXiv:2311.12198 (2023)
- [64] Yang, Y., Jia, B., Zhi, P., Huang, S.: Phycene: Physically interactable 3d scene synthesis for embodied ai (2024)
- [65] Yao, Y., Luo, Z., Li, S., Fang, T., Quan, L.: Mvsnet: Depth inference for unstructured multi-view stereo. In: European Conference on Computer Vision (ECCV). pp. 767–783 (2018)
- [66] Yao, Y., Luo, Z., Li, S., Shen, T., Fang, T., Quan, L.: Recurrent mvsnet for high-resolution multi-view stereo depth inference. In: Conference on Computer Vision and Pattern Recognition (CVPR). pp. 5525–5534 (2019)
- [67] Yariv, L., Gu, J., Kasten, Y., Lipman, Y.: Volume rendering of neural implicit surfaces. In: Advances in Neural Information Processing Systems (NeurIPS) (2021)

- [68] Yeshwanth, C., Liu, Y.C., Nießner, M., Dai, A.: Scannet++: A high-fidelity dataset of 3d indoor scenes. In: International Conference on Computer Vision (ICCV) (2023)
- [69] Yu, Z., Peng, S., Niemeyer, M., Sattler, T., Geiger, A.: Monosdf: Exploring monocular geometric cues for neural implicit surface reconstruction. In: Advances in Neural Information Processing Systems (NeurIPS) (2022)
- [70] Yuan, Y., Song, J., Iqbal, U., Vahdat, A., Kautz, J.: Physdiff: Physics-guided human motion diffusion model. In: International Conference on Computer Vision (ICCV) (2023)
- [71] Yuan, Y., Wei, S.E., Simon, T., Kitani, K., Saragih, J.: Simpoe: Simulated character control for 3d human pose estimation. In: Conference on Computer Vision and Pattern Recognition (CVPR). pp. 7159–7169 (2021)
- [72] Zhang, C., Cui, Z., Zhang, Y., Zeng, B., Pollefeys, M., Liu, S.: Holistic 3d scene understanding from a single image with implicit representation. In: Conference on Computer Vision and Pattern Recognition (CVPR) (2021)
- [73] Zhang, K., Riegler, G., Snavely, N., Koltun, V.: Nerf++: Analyzing and improving neural radiance fields. arXiv preprint arXiv:2010.07492 (2020)
- [74] Zhu, Y., Gao, T., Fan, L., Huang, S., Edmonds, M., Liu, H., Gao, F., Zhang, C., Qi, S., Wu, Y.N., et al.: Dark, beyond deep: A paradigm shift to cognitive ai with humanlike common sense. *Engineering* **6**(3), 310–345 (2020)